A&A 664, A44 (2022)
https://doi.org/10.1051/0004-6361/202244089

Astronomy & Astrophysics

The evolution of the H_2O maser emission in the accretion burst source G358.93−0.03⋆

O. S. Bayandina[1], C. L. Brogan[2], R. A. Burns[3,4,5], A. Caratti o Garatti[6,7], J. O. Chibueze[8,9], S. P. van den Heever[10], S. E. Kurtz[11], G. C. MacLeod[10], L. Moscadelli[1], A. M. Sobolev[12], K. Sugiyama[13,4], I. E. Val'tts[14], and Y. Yonekura[15]

[1] INAF – Osservatorio Astrofisico di Arcetri, Largo E. Fermi 5, 50125 Firenze, Italy
e-mail: olga.bayandina@inaf.it
[2] National Radio Astronomy Observatory, 520 Edgemont Road, Charlottesville, VA 22903, USA
[3] Joint Institute for VLBI ERIC, Oude Hoogeveensedijk 4, 7991 PD Dwingeloo, The Netherlands
[4] Mizusawa VLBI Observatory, National Astronomical Observatory of Japan, 2-21-1 Osawa, Mitaka, Tokyo 181-8588, Japan
[5] Korea Astronomy and Space Science Institute, 776 Daedeokdae-ro, Yuseong-gu, Daejeon 34055, Republic of Korea
[6] INAF – Osservatorio Astronomico di Capodimonte, via Moiariello 16, 80131 Napoli, Italy
[7] Dublin Institute for Advanced Studies, School of Cosmic Physics, Astronomy & Astrophysics Section, 31 Fitzwilliam Place, Dublin 2, Ireland
[8] Space Research Unit, Physics Department, North-West University, Potchefstroom 2520, South Africa
[9] Department of Physics and Astronomy, University of Nigeria, Carver Building, 1 University Road, Nsukka 410001, Nigeria
[10] SARAO, Hartebeesthoek Radio Astronomy Observatory, PO Box 443, Krugersdorp 1741, South Africa
[11] Instituto de Radioastronomía y Astrofísica, Universidad Nacional Autónoma de México, Antig. Carr. a Patzcuaro 8701, Morelia 58089, Mexico
[12] Ural Federal University, 51 Lenin Str., 620051 Ekaterinburg, Russia
[13] National Astronomical Research Institute of Thailand (Public Organization), 260 Moo 4, T. Donkaew, A. Maerim, Chiang Mai 50180, Thailand
[14] Astro Space Center, P.N. Lebedev Physical Institute of RAS, 84/32 Profsoyuznaya st., Moscow 117997, Russia
[15] Center for Astronomy, Ibaraki University, 2-1-1 Bunkyo, Mito, Ibaraki 310-8512, Japan

Received 23 May 2022 / Accepted 15 June 2022

ABSTRACT

Context. The massive young stellar object (MYSO) G358.93−0.03-MM1 showed an extraordinary near-infrared- to (sub-)millimetre-dark and far-infrared-loud accretion burst, which is closely associated with flares of several class II methanol maser transitions, and, later, a 22 GHz water maser flare.
Aims. Water maser flares provide an invaluable insight into ejection events associated with accretion bursts. Although the short timescale of the 22 GHz water maser flare made it impossible to carry out a very long baseline interferometry observation, we could track it with the *Karl G. Jansky* Very Large Array (VLA).
Methods. The evolution of the spatial structure of the 22 GHz water masers and their association with the continuum sources in the region is studied with the VLA during two epochs, pre- and post-H_2O maser flare.
Results. A drastic change in the distribution of the water masers is revealed: in contrast to the four maser groups detected during epoch I, only two newly formed clusters are detected during epoch II. The 22 GHz water masers associated with the bursting source MM1 changed in morphology and emission velocity extent.
Conclusions. Clear evidence of the influence of the accretion burst on the ejection from G358.93−0.03-MM1 is presented. The accretion event has also potentially affected a region with a radius of ∼2″ (∼13 500 AU at 6.75 kpc), suppressing water masers associated with other point sources in this region.

Key words. stars: massive – stars: evolution – stars: formation – stars: jets – masers – stars: individual: G358.93−0.03

1. Introduction

Disk-mediated accretion accompanied by episodic accretion bursts is thought to be a common mechanism of both low- and high-mass star formation (e.g., Crimier et al. 2010; Meyer et al. 2019). However, in the case of high-mass protostars, this phenomenon is poorly studied as it has only recently been discovered (Caratti o Garatti et al. 2017). Little observational evidence exists, and only four accretion bursts in massive young stellar objects (MYSOs) have been detected and analysed so far (Caratti o Garatti et al. 2017; Hunter et al. 2017; Proven-Adzri et al. 2019; MacLeod et al. 2021; Stecklum et al. 2021). Recent studies show that maser monitoring can identify and trace high-mass young stellar objects (YSOs) at the very important, yet very short, phase of accretion bursts (e.g., Szymczak et al. 2018; MacLeod et al. 2018, 2019; Brogan et al. 2019; Breen et al. 2019).

G358.93−0.03-MM1, located at the near kinematic distance of $6.75^{+0.37}_{-0.68}$ kpc (Reid et al. 2014), showed an extraordinary near-infrared- to (sub-)millimetre-dark and far-infrared-loud MYSO accretion burst in 2019 (Stecklum et al. 2021). The

⋆ Full Table 4 is only available at the CDS via anonymous ftp to cdsarc.u-strasbg.fr (130.79.128.5) or via http://cdsarc.u-strasbg.fr/viz-bin/cat/J/A+A/664/A44

G358.93−0.03 region is densely populated, and Brogan et al. (2019) resolved the protocluster into eight (sub-)millimetre continuum sources designated as MM1-MM8 in order of decreasing right ascension (RA). The continuum source G358.93−0.03-MM1 shows characteristics of an extremely young massive object (Stecklum et al. 2021). The circumstellar disk around MM1 is found to be unusually low-mass for an MYSO, and the accretion burst in the source is the least energetic one out of the limited sample of such events in MYSOs (Stecklum et al. 2021).

The study of the maser emission during the burst performed by the Maser Monitoring Organization (M2O[1]; a global community for maser-driven astronomy; Burns et al. 2022) has provided the most complete picture of an accretion burst in MYSOs to date (MacLeod et al. 2019; Brogan et al. 2019; Breen et al. 2019; Burns et al. 2020; Stecklum et al. 2021; Bayandina et al. 2022). The MM1 burst was accompanied with flares of maser emission (e.g., Sugiyama et al. 2019; MacLeod et al. 2019; Brogan et al. 2019; Breen et al. 2019; Bayandina et al. 2022). Among the detected masers were rare and even previously undiscovered methanol maser transitions, some of which were unpredicted (MacLeod et al. 2019; Breen et al. 2019; Brogan et al. 2019). We note that the maser flare in the source was detected by the M2O first (Sugiyama et al. 2019; MacLeod et al. 2019; Brogan et al. 2019; Breen et al. 2019) and only later was the study of the infrared data able to confirm the accretion burst (Stecklum et al. 2021).

Interferometric observations, conducted after the methanol maser flare, revealed the presence of an accretion disk and were able to follow the propagation of a heatwave across it (Burns et al. 2020; Chen et al. 2020; Bayandina et al. 2022). The next important step was to study the spatial structure of the water maser. Accretion and ejection are known to be closely associated – brightening outflow cavities (Caratti o Garatti et al. 2017), flares of H_2O masers likely tracing jets (Chibueze et al. 2021), and radio jet bursts (Cesaroni et al. 2018) have been reported after accretion bursts.

Due to the short duration of the water maser flare in G358.93−0.03, no very long baseline interferometry (VLBI) observations were made, and the low flux density of the H_2O maser outside of the flare made it difficult to image with VLBI. However, the faint water maser emission is readily detectable by the *Karl G. Jansky* Very Large Array (VLA). With the high sensitivity and moderate resolution of the VLA, we were able to study the spatial structure of the H_2O masers before and after the maser flares. Additionally, with the VLA we were able to study the centimetre-continuum sources in the region.

2. Observations and data reduction

2.1. VLA observations

The observation of G358.93−0.03 was conducted with the *Karl G. Jansky* VLA in two sessions: epoch I on February 25, 2019 (project code 19A-448, C → B configuration), and epoch II on June 4, 2019 (19A-476, A configuration). The H_2O maser flare in G358.93−0.03 took place in April 2019 (Fig. 3), and thus the VLA epoch I observations of February 2019 are considered as the H_2O maser pre-flare epoch and the epoch II observations of June 2019 as the post-flare epoch.

The general technical details of the observations are described in Bayandina et al. (2022). Here we mention only the parameters of the water maser study.

[1] https://www.masermonitoring.org/

The observation parameters of continuum and water maser data are presented in Tables 1 and 2, respectively. To observe continuum emission, we used 31 spectral windows of 128 1 MHz channels in the *C*, *Ku*, and *K* bands. The maser line was observed in a 4 MHz spectral window of 1024 channels. Detection of continuum and maser emission in each band and epoch is marked with 'Y'; non-detection is marked with 'N'.

Data reduction was performed as described in Bayandina et al. (2022). Here we repeat two remarks detailed in Bayandina et al. (2022): (1) the observations were made during a multi-frequency maser flare that led to a leakage of a few maser lines into continuum spectral windows (see the notes in Table 1); (2) a positional shift was introduced into the maser data to compensate for a discrepancy in the absolute coordinates of the maser and continuum data obtained with different facilities and beams; for example, the maser data obtained with the VLA in the present work is compared with the Atacama Large Millimeter/submillimeter Array (ALMA) data from Brogan et al. (2019).

2.2. HartRAO monitoring

The single-dish monitoring results reported here were made using the 26 m telescope at the Hartebeesthoek Radio Astronomy Observatory (HartRAO)[2]. The 1.3 cm receiver is a dual, left and right circularly polarised, cryogenically cooled receiver. It was calibrated relative to Hydra A, 3C123, and Jupiter assuming the flux scale of Ott et al. (1994). Observations were recorded with a 1024-channel (per polarisation), 1.0 MHz bandwidth spectrometer. Frequency switching was employed as were half-power beamwidth pointing correction observations for all epochs of observation. The total velocity extent of each observation is 54 km s^{-1}, and the resolution is 0.105 km s^{-1}. The observing frequency is 22 235.120 MHz, and this is corrected for the local standard of rest (LSR) velocity $v_{\rm LSR} = -17$ km s^{-1}. Each epoch of observation comprises two six-minute observations with a sensitivity of ∼0.1 K or ∼1 Jy per polarisation. The beamwidth is 2.2′. More information regarding this receiver and the observing method employed is given in MacLeod et al. (2018). Monitoring began on January 20, 2019, and observations were made every 10 to 20 days, subject to other scheduled observing.

3. Results

3.1. Continuum emission

To provide context for the discussion of the water maser spatial distribution, we first present the continuum sources detected in the region.

Our VLA observations towards G358.93−0.03 detected two continuum sources associated with the hot cores MM1 and MM3 discovered in Brogan et al. (2019). The obtained VLA images are shown in Fig. 1, and a summary of the detected source parameters is presented in Table 3.

MM1 is the brightest millimetre-continuum source, the most line-rich hot core in the region, and the source of the accretion burst (Brogan et al. 2019). As described in Bayandina et al. (2022), MM1 was detected only in the *K* band during the first epoch of the VLA observations.

The continuum source detected in all three frequency bands with the VLA is associated with the ALMA hot core MM3

[2] See http://www.hartrao.ac.za/spectra/ for further information.

Table 1. Observation parameters: continuum.

Bands [a]	Freq. (GHz)	Epoch	Int. Time (min)	Synth. Beam (arcsec)	PA (°)	1σ rms [b] (μJy beam^{-1})	Detect. MM1 [c]	Detect. MM3 [c]
C [1]	6.0	I	14	4.66 × 0.77	+9.02	23	N	Y
		II	16	2.61 × 1.05	−0.07	23	N	Y
Ku [2]	15.0	I	16	1.84 × 0.46	+3.29	11	N	Y
		II	16	1.12 × 0.45	−6.32	13	N	Y
K [3]	20.0	I	32	1.28 × 0.30	+0.28	16	Y	Y
		II	19	0.78 × 0.32	−9.98	15	N	N

Notes. [a]The following maser lines were detected in the continuum windows (the listed lines were flagged during the data processing to avoid false detections in the continuum images): (1) 6.18, 6.67, 7.68, and 7.83 GHz; (2) 14.30 GHz; (3) 20.97 and 20.35 (epoch I only) GHz. [b]The detection threshold is set to the 3σ level. [c]Hereinafter we adopt the source naming from Brogan et al. (2019).

Table 2. Observation parameters: spectral line.

Band	Transition	Freq. (MHz)	Epoch	Int. Time (min)	Synth. Beam (arcsec)	PA (°)	Spec. res. (km s^{-1})	1σ rms (mJy beam^{-1})	Detection
K	H_2O $6_{1,6} \rightarrow 5_{2,3}$	22 235.08	I	16	1.04 × 0.21	+0.64	0.05	14	Y
			II	19	0.57 × 0.24	−8.35	0.11	17	Y

(Brogan et al. 2019). The *C*-band epoch I detection is marginal, as it barely meets the 3σ threshold. The ALMA and VLA positions of MM3 differ by ∼0.3″ (Fig. 2), which is similar to the absolute positional uncertainty reported in Brogan et al. (2019). The VLA and ALMA (Brogan et al. 2019) studies of MM3 flux density were done in the period of high activity in the region, which means we cannot directly compare the millimetre and centimetre fluxes.

No continuum emission above the 3σ noise level is detected during VLA epoch II in the *K* band.

3.2. Water masers

3.2.1. HartRAO monitoring

The flare of the water emission in G358.93−0.03 was short-lived (each flare had a duration of about a day) and moderate (the maximum flux was ∼20 Jy). In contrast, the previously known accretion bursts in the MYSOs NGC 6334I-MM1 and S255 NIRS 3 showed long-lasting flares (timescales of a year to a few years) of strong (kJy) H_2O masers (MacLeod et al. 2018; Hirota et al. 2021).

The methanol masers in G358.93−0.03-MM1 flared in February-March of 2019 (MacLeod et al. 2019; Brogan et al. 2019; Breen et al. 2019), but the water maser remained stable during this period, with a flux density of ∼1 Jy (see Fig. 3). In April 2019, the single-dish telescopes participating in the M2O monitoring of G358.93−0.03 detected a rapid and steady growth of the water maser flux density. By April 19, the spectral feature at V_{LSR} = −17.42 km s^{-1} reached ∼26 Jy (Fig. 3). Two more flares of the H_2O maser emission were noticed later. On May 14, 2019, the two spectral features at V_{LSR} = −13.31 km s^{-1} and V_{LSR} = −18.58 km s^{-1} flared simultaneously, reaching a flux density of 21 and 19 Jy, respectively. On May 23, 2019, the last case of enhanced activity of the water maser was detected when the spectral feature at V_{LSR} = −13.42 km s^{-1} increased its flux to 22 Jy (the M2O monitoring; Fig. 3).

3.2.2. VLA

The H_2O maser spectra detected towards G358.93−0.03 during VLA epochs I and II differ significantly from each other (see the left panels of Fig. 4). During VLA epoch I, the H_2O emission covered the velocity range from ∼−21 to −16 km s^{-1}, and during epoch II from ∼−23 to −13 km s^{-1}. During both epochs, three ∼1 Jy spectral features populate the spectra; however, their peak velocities are different. The epoch I peaks are at V_{LSR} = −19.9, −18.8, and −17.0 km s^{-1}, while the epoch II peaks are at V_{LSR} = −21.5, −19.6, and −13.8 km s^{-1}. Notably, during the post-flare epoch (VLA epoch II) there is no emission at the velocity of the flaring spectral feature (Fig. 4).

The position, velocity, and integrated and peak flux density of each of the detected 22 GHz water maser spots[3] are listed in Table 4. The spot maps presented in the paper are based on Table 4. We note that the warning about the limitation of the interpretation of spatial structures visible on the VLA spot maps from Bayandina et al. (2022) applies to the water maser data as well. In particular, even though the achieved signal-to-noise ratio allows us to fit the maser spot positions with sub-beamsize accuracy (Table 4) and the structures seen in the water maser spot maps are much smaller than the synthesized VLA beam (Table 2), the spatial and velocity structure may be dominated by the brighter components. The presented spot maps provide a general view of the spatial and velocity distribution of the water maser emission, but higher resolution observations are required to confirm the detected patterns.

The spatial distribution of the detected H_2O masers is found to differ significantly from the methanol masers detected with the VLA during the same observing sessions and described in Bayandina et al. (2022). The water maser emission covers a larger area of about 3″ (Figs. 4 and 5), while the methanol emission was detected in a region of ∼0.2″ in the vicinity of MM1 only.

[3] In the following, we use the term ‘maser spots’ to refer to maser emissions detected in a single velocity channel of a data cube.

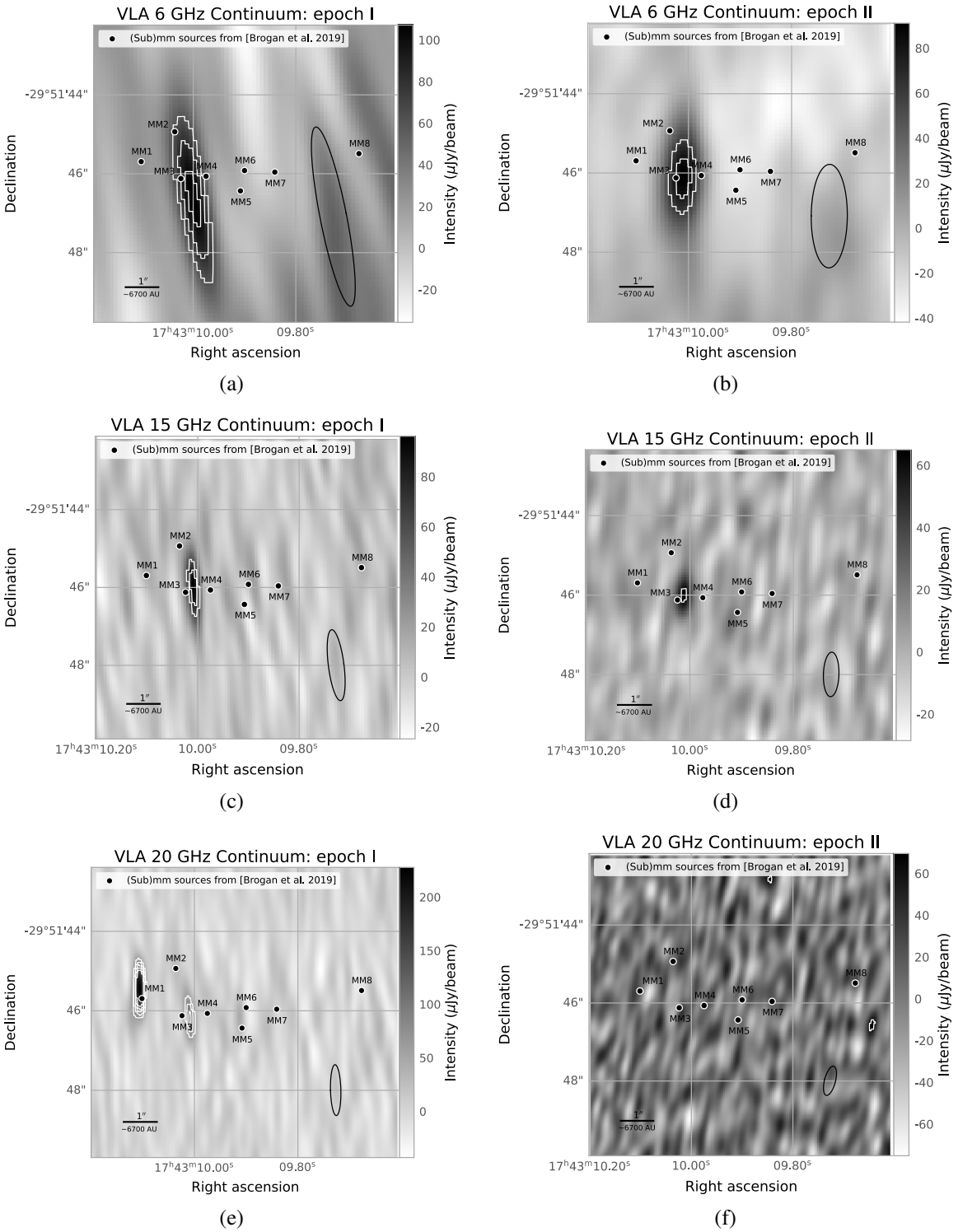

Fig. 1. VLA continuum images of G358.93−0.03 at 6, 15, and 20 GHz during epochs I (*left panels*) and II (*right panels*). The contour levels are [6, 8, 10] × 10 μJy beam^{-1}. The black dots mark the positions of the (sub-)millimetre sources from Brogan et al. (2019). The synthesized VLA beam size of each image is shown with the black ellipses in the lower-right corner of the panels.

During epoch I, the spatial distribution of the H_2O masers consists of four spatial components (Figs. 4–5a): Component I-1 is found in the vicinity of MM1 and hosts maser spots with a velocity range from ∼−17.5 to −20 km s^{-1}. Component I-2 is the brightest water maser in the region. It is located ∼1″ to the NW of MM1 and is spatially associated with the continuum source MM2. Maser spots detected in component I-2 have the same velocities as those of component I-1. Components I-3 and I-4 are found to the SW of MM1 and are associated with the continuum sources MM4 and MM5, respectively, detected in Brogan et al. (2019). Component I-3 consists of the maser spots with velocities of ∼−17 km s^{-1}, and component I-4 shows velocities of ∼−20 km s^{-1}. Thus, during epoch I water masers are observed towards all the strongest millimetre sources, except

Table 3. VLA continuum emission peak parameters.

Association	Bands	Epoch	RA(J2000) ($^h\,^m\,^s$)	Dec.(J2000) ($^\circ\,'\,''$)	Integrated flux (μJy)	Peak flux (μJy beam^{-1})	S/N
MM3	*C*	I	17:43:10.005(0.113) [(a)]	−29:51:45.90(0.68) [(a)]	263(76)	170(26)	3
		II	17:43:10.007(0.003)	−29:51.46:35(0.26)	83(26)	98(14)	4
	Ku	I	17:43:10.004(0.001)	−29:51:46.27(0.17)	132(27)	109(11)	11
		II	17:43:10.007(0.002)	−29:51:46.30(0.07)	113(19)	84(9)	8
	K	I	17:43:10.009(0.0004)	−29:51:46.03(0.06)	133(14)	111(6)	11

Notes. [(a)]The positional uncertainties are statistical errors of fit.

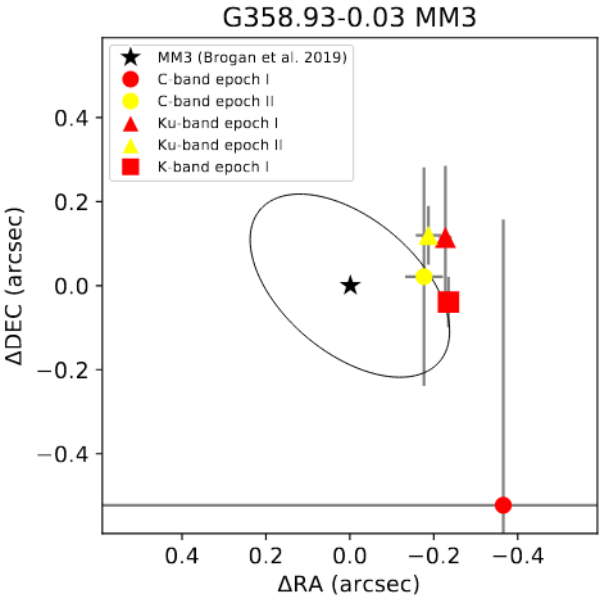

Fig. 2. Centimetre-continuum (this work) and millimetre-continuum (Brogan et al. 2019) peak position of MM3. The *C*- (circle), *Ku*- (triangle), and *K*-band (square) peaks detected with the VLA during epoch I are shown in red, and during epoch II in yellow. The ellipse represents the size estimation of MM3 obtained in Brogan et al. (2019). The grey error bars indicate the position fitting errors from Table 3.

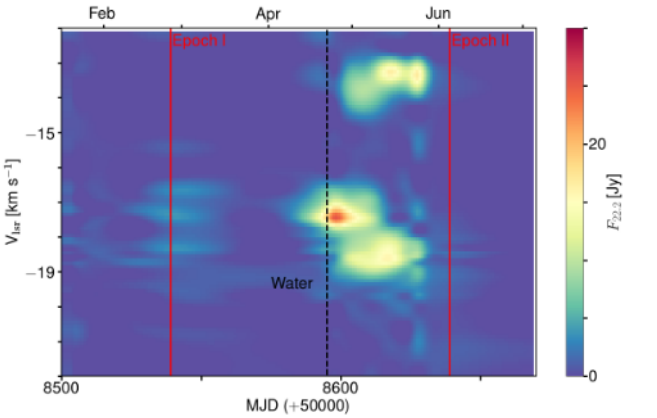

Fig. 3. Dynamic spectrum of the 22 GHz water maser emission in G358.93−0.03 for the period January–July 2019. The black dotted line indicates the flare of the water maser. The red lines indicate the dates of the VLA epoch I and II observations (M2O data: the HartRAO 26 m telescope monitoring program).

MM3, which is the only source with associated continuum emission.

In contrast, only two H_2O maser components are detected during VLA epoch II (Figs. 4–5b): Component II-1 is found at the same position as component I-1, close to the line-rich source MM1, but the spectrum of component II-1 has a wider velocity range and spans from ∼−13.5 to −20.5 km s^{-1}. No emission is detected at the position of component I-2. Component II-3-4 is located between the positions of components I-3 and I-4 and, consequently, between the continuum sources with which these water masers were associated, MM4 and MM5. The component consists of maser spots with velocities of ∼−21 to −22 km s^{-1}. No features with these velocities were detected during epoch I.

3.2.3. Water masers associated with MM1

The bursting source MM1 showed water maser emission during both VLA epochs, though the distribution of the maser spots changed significantly between the observations.

During epoch I, the maser spots composing component I-1 spread from MM1 to the north (Fig. 6). The cluster has a linear structure with a length of ∼0.2″ and a width of only ∼0.05″. No clear velocity gradient is found. The distribution of the maser spots resembles the pre-H_2O maser flare state detected in the source with the VLA B-configuration on April 4, 2019, and reported in Chen et al. (2020). However, while the general spatial distribution is preserved, the velocity range of the water maser emission detected in Chen et al. (2020) was broader (V_{LSR} from ∼−16 to ∼−23 km s^{-1}).

In contrast to epoch I, the 22 GHz water maser cluster II-1 is distributed on both sides of MM1 and elongated 0.2″ in the NW-SE direction (Fig. 6). It shows a velocity gradient similar to the one found for the methanol masers in Bayandina et al. (2022): blueshifted maser spots are displaced to the north and redshifted spots to the south.

3.2.4. Water masers associated with MM2, MM4, and MM5

Water masers, spatially associated with the continuum sources MM2 and MM4, are found during VLA epoch I only (Fig. 7). The water masers in the vicinity of MM5 are found during both epochs (Figs. 7 and 8) but show significant spatial shift.

The H_2O masers associated with MM2, component I-2, are located ∼0.15″ to the NE of the continuum source. The maser spots correspond to two spectral features at velocities of −18.8 and −17.5 km s^{-1} and form two close, but clearly spatially separated, clusters. The cluster at velocities of about −19 km s^{-1} is located closer to MM2 and is linearly elongated in the N-S direction. The other cluster at about −17 km s^{-1} is separated

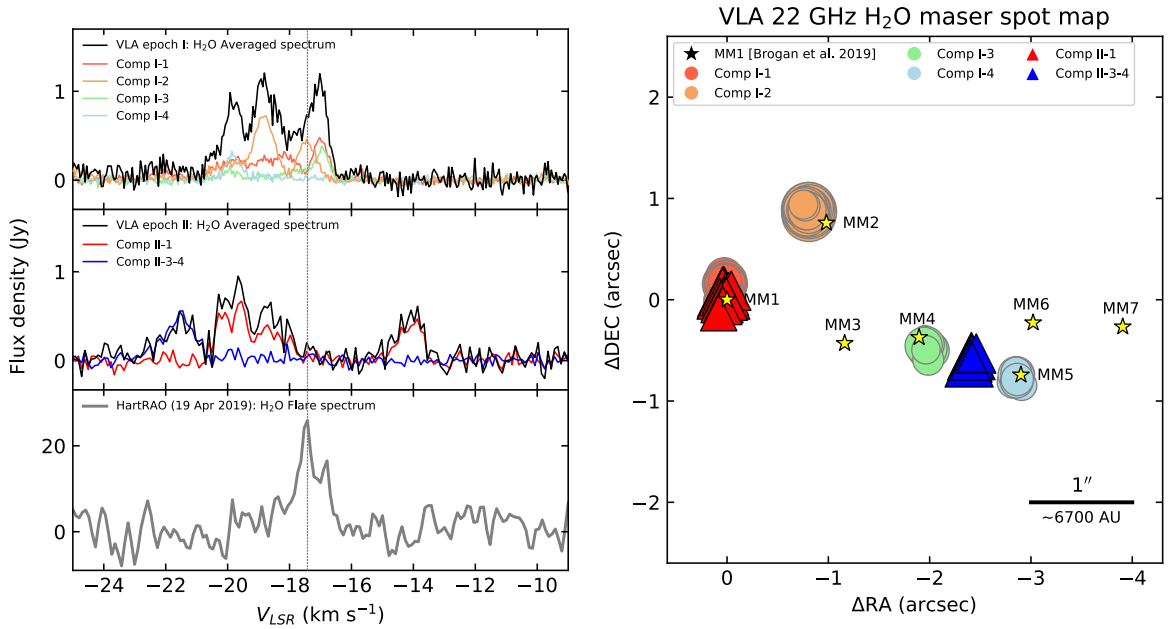

Fig. 4. Comparison of the 22 GHz H_2O maser emission detected with the VLA during epochs I and II. *Left panels:* spectra of the H_2O maser components (marked by colour; see the legend) and total spectrum (black line) detected with the VLA during epoch I *(top)* and epoch II *(middle)*. *Bottom panel*: maser flare spectrum obtained with the HartRAO 26 m telescope on April 19, 2019. The dashed line indicates the peak velocity of the flare spectrum. *Right panel:* combined H_2O maser spot map. The epoch I maser spots are marked by light-coloured circles; the epoch II maser spots are marked by bright-coloured triangles. Positional offsets are relative to MM1 (Brogan et al. 2019). The position of the continuum emission detected with the VLA and associated with MM3 (Brogan et al. 2019) is marked by a black cross.

Table 4. 22 GHz H_2O maser parameters.

Component	RA (J2000) ($^h\,^m\,^s$)	Dec (J2000) ($^\circ\,'\,''$)	Integrated flux (mJy)	Peak flux (mJy beam^{-1})	V_{LSR} (km s^{-1})
I-1	17:43:10.1037 ± 0.0001	−29:51:45.609 ± 0.038	235 ± 22	222 ± 9.1	−20.13
	17:43:10.1018 ± 0.0002	−29:51:45.579 ± 0.039	175 ± 22	201 ± 10	−20.08
	17:43:10.1026 ± 0.0002	−29:51:45.585 ± 0.041	231 ± 23	224 ± 9.4	−20.02

Notes. (1) Table 4 is published in its entirety in machine-readable format. A portion is shown here for guidance regarding its form and content. (2) The positional shifts of ΔRA = −0.02, ΔDec = −0.02 (epochs I and II) were introduced to the data to prepare the figures (see Sect. 2).

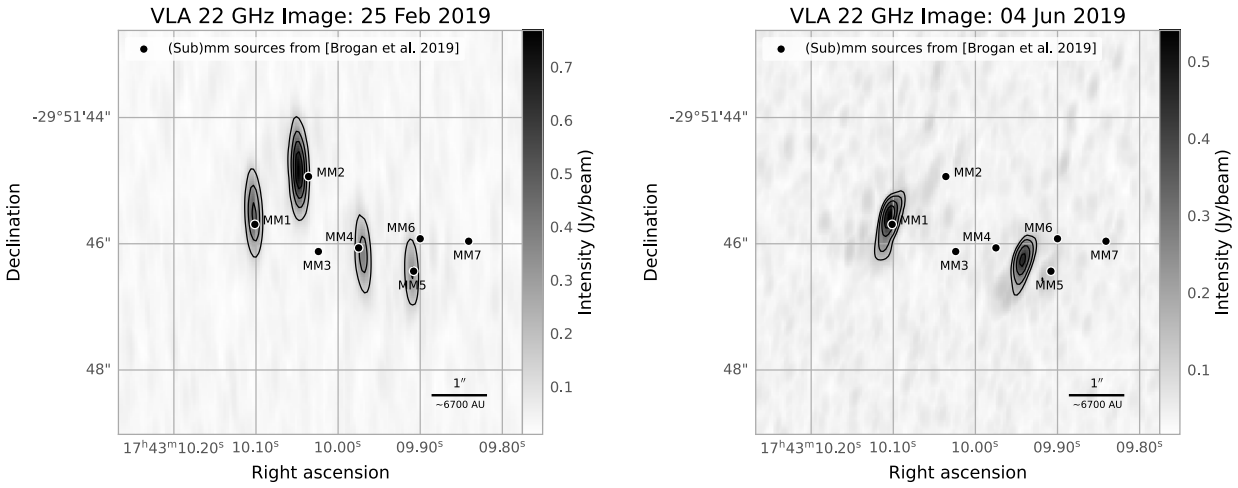

Fig. 5. 22 GHz H_2O maser emission detected in G358.93−0.03 with the VLA during (a) epoch I and (b) epoch II.

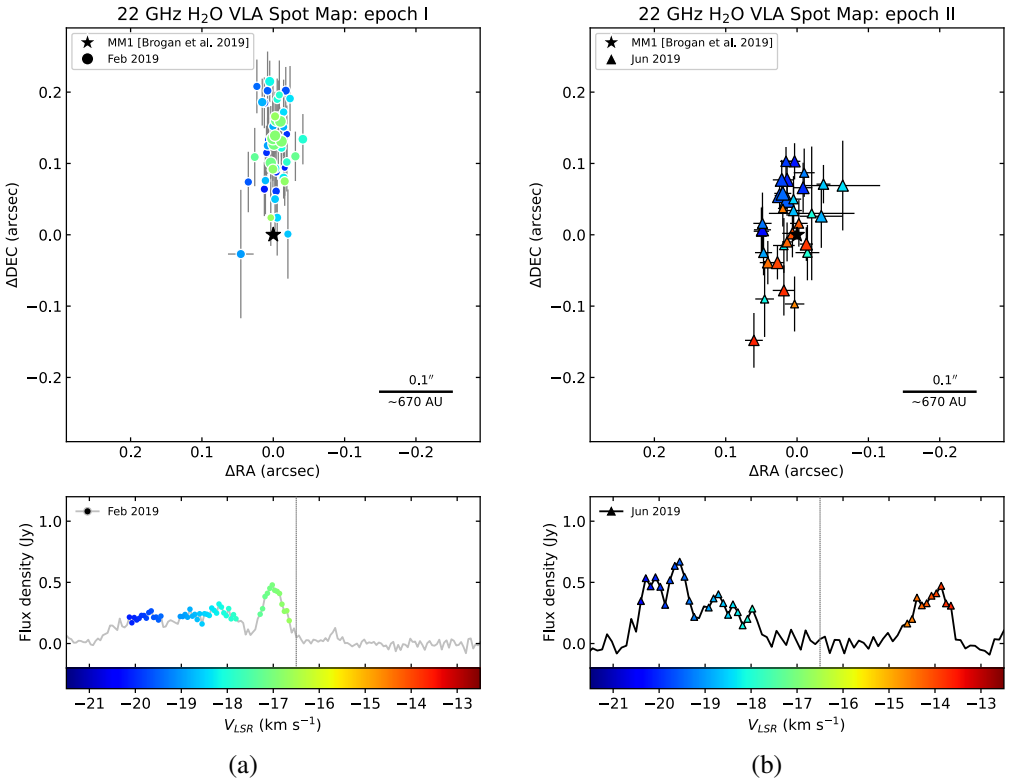

(a) (b)

Fig. 6. 22 GHz water maser spot maps and spectra of component I-1 from epoch I and component II-1 from epoch II. The plots are colour-coded by radial velocity (see the colour bar for the colour scale). The markers on the spectra correspond to the maser spots on the map. The diameter of each spot is proportional to the flux. The error bars indicate the position fitting errors from Table 4. Positional offsets are relative to the MM1 position (star marker) from Brogan et al. (2019). The dashed line in the spectrum panels marks the centre velocity of MM1 (Brogan et al. 2019).

more from MM2 and shows a linearly elongated structure and an orientation similar to the previous one.

Component I-3 is located ∼0.1″ SW of MM4. The cluster is linearly elongated with a size of ∼0.2″.

The water maser emission of component I-4 is found close to MM5 and linearly elongated ∼0.1″ to the south. Similar to component I-1, it is closely associated with its continuum source. Component I-4 is the least crowded and consists of fewer than a dozen maser spots.

Component II-3-4 is the only water maser besides component II-1 detected during VLA epoch II. Its peak velocity is about −21.5 km s^{-1}. The component is located at about the same separation of ∼0.48″ from the positions of MM4 and MM5, but based on the maser spots' velocity and cluster orientation, it seems to be associated with MM5. The cluster appears as a bow-shaped structure elongated in the NW-SW direction, with a curvature radius that corresponds approximately to the direction towards MM5.

4. Discussion

4.1. Ejection activity of the accretion burst source MM1

The narrow, elongated spatial structure of the water maser clusters detected in the vicinity of MM1 (components I-1 and II-1; Fig. 6) as well as their location relative to the accretion disk traced by the methanol masers (Fig. 9) suggest their association with a jet or outflow powered by MM1. Considering the low flux density (∼1 Jy) of the water maser emission and the size of the maser clusters (∼0.2″) detected during two VLA epochs, the jet seems to be at an early phase of activity. However, we must note that H_2O masers are not good tracers of jet size as they trace only the densest portion of it.

One feature of the source, which has complicated the study of the ejection caused by the accretion burst, is the orientation of the source in the plane of the sky. A face-on accretion disk around MM1 was detected by the methanol maser observations (Burns et al. 2020; Chen et al. 2020; Bayandina et al. 2022). The orientation of the disk allowed us to trace the propagation of the burst heatwave and to penetrate the fine structure of the disk, which turned out to be composed of spiral arm structures (Chen et al. 2020; Bayandina et al. 2022). However, assuming the axis of the outflow to be perpendicular to the disk, the outflow projection effect to the plane of the sky means that the blueshifted and redshifted outflows are largely coincident. Our VLA H_2O maser results (especially epoch II; see Fig. 6), which show partial spatial overlap between the blueshifted and redshifted maser features, support our suggested orientation of the outflow along the line-of-sight to the source.

Since both H_2O masers and SiO emission are typical tracers of outflow activity, we compared our VLA observations with archive ALMA data (Project: 2019.1.00768.S) of SiO J = 5–4 emission in the region (Fig. 10). The SiO image was obtained with the angular resolution of ∼0.3″, combining two ALMA datasets from 2019 (October 1 and 7) and one from 2021 (April 1). The ALMA SiO emission associated with MM1 shows a compact structure with a size of ∼0.7″ (corresponding to ∼4700 AU at the distance of 6.75 kpc) in all channels (see Fig. 10). A more detailed analysis of the properties of the outflows in the region based on ALMA data will be presented in Brogan et al. (in prep.).

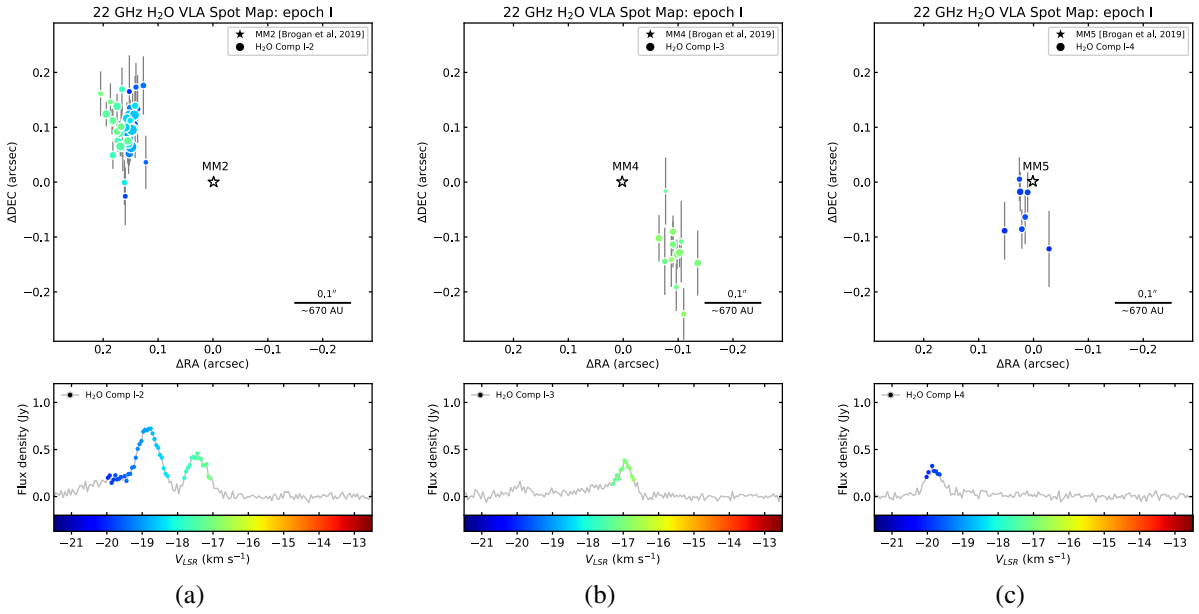

Fig. 7. 22 GHz water maser spot maps and spectra of components (a) I-2, (b) I-3, and (c) I-4 from epoch I. The plots are colour-coded by radial velocity (see the colour bars for the colour scale). The markers on the spectra correspond to the maser spots on the map. The diameter of each spot is proportional to the flux. The positional offsets are relative to the (a) MM2, (b) MM4, and (c) MM5 (star markers) positions from Brogan et al. (2019).

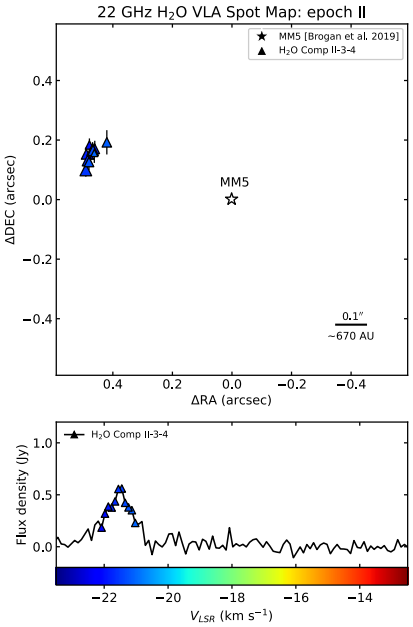

Fig. 8. 22 GHz water maser spot map and spectrum of component II-3-4 from epoch II. The plot is colour-coded by radial velocity (see the colour bar for the colour scale). The markers on the spectrum correspond to the maser spots on the map. The diameter of each spot is proportional to the flux. The positional offsets are relative to the MM5 position (star marker) from Brogan et al. (2019).

The evolution of the water maser structure between the two VLA observation epochs (Fig. 6) was assumed to be excited by an enhanced radiation field caused by the accretion event, and not a mechanical matter transfer of the circumstellar medium. The southern part of the H_2O maser emission with the redshifted velocities has a size of ∼0.1″ and was detected during VLA epoch II only. If we assume the presence of a physical matter movement that travelled ∼0.1″ (or ∼670 AU at the distance of 6.75 kpc) in 99 days between VLA epochs I and II, it must have had a speed of 0.01c. Such speeds are too high for the survival of molecules, including H_2O. Therefore, it is more likely that the water masers detected during the first observation epoch dimmed, and the new masers, detected during the second epoch, were excited by the heating of the medium by the arrived radiation with proper spectral properties. Such a scenario was proposed for NGC 6334 I (Sobolev et al. 2019; Brogan et al. 2018).

4.2. Large-scale effect of the accretion burst told by H_2O masers

Our VLA images have revealed drastic changes in the distribution of the water masers in the whole region and not only around the bursting source MM1. Of the three clusters detected during the first VLA epoch and associated with MM2, MM4, and MM5, only one associated with MM5 remained after the burst (Fig. 5).

The arc-shaped morphology of component I-2 (Fig. 7) suggests its association with outflow activity in the vicinity of MM2 (e.g., Burns et al. 2017). Under this assumption, the water masers trace bow-shaped shocks expanding from the central source, MM2. Two separate 'layers' of the shock are highlighted by the water masers. The layers overlap spatially (within uncertainties) but are clearly separated in terms of velocity. The brighter layer (∼0.8 Jy) has a bluer $V_{\rm LSR}$ of ~ -19 km s^{-1}, and the fainter layer (∼0.5 Jy) has a redder $V_{\rm LSR}$ of ~ -17.5 km s^{-1}. We note that the MM2 region shows weak SiO emission (Fig. 10). The component was the brightest water maser in the region during epoch I, but it became undetectable during epoch II. The change in the flux density can be attributed to the high variability of the water maser, which, coupled with the described morphology of the component, suggests that MM2 is the driving source of a young and active jet or outflow. On the other hand, the spectral feature at $V_{\rm LSR} = -17.42$ km s^{-1} of component I-2 precisely coincides in terms of velocity with the peak of the water maser flare (see Fig. 4). Based on this curious coincidence,

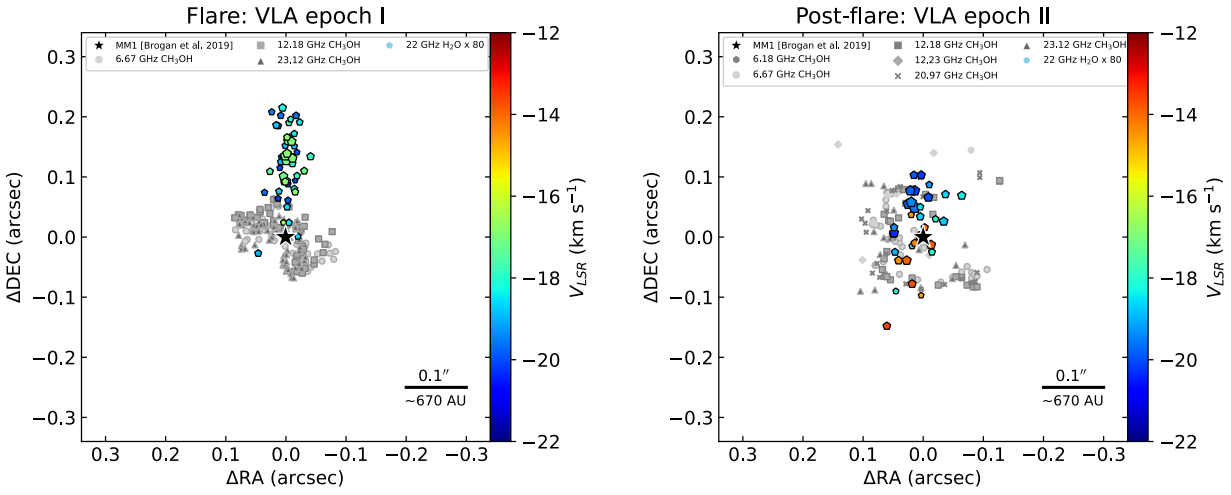

Fig. 9. Comparison of spatial distribution of the methanol from Bayandina et al. (2022) and water maser emission detected in G358.93−0.03 during the (a) flare (VLA epoch I) and (b) post-flare (VLA epoch II) epochs. Positional offsets are relative to the MM1 position from Brogan et al. (2019) (star marker).

we can speculate that the strongest water maser flare, detected on April 22, 2019, may have been caused by an increase in the brightness of the water masers in the vicinity of MM2. Unfortunately, the lack of knowledge about the spatial distribution of water masers in the source at the time of the flare prevents us from verifying this assumption.

A bright and extended peak of the SiO emission is found in the vicinity of MM4. While the SiO emission suggests the presence of outflow activity associated with the continuum source, the water maser component I-3 is faint (∼0.5 Jy) and detected only during epoch I. The elongated structure of the water maser might be associated with a jet or outflow. The SiO and water maser emission trace shock activity on different sides of MM4: the axis of the SiO outflow is oriented to the NE, while the water maser jet or outflow axis points to the SW. Based on the SiO image, MM4 seems to be one of the most active outflow sources in the region.

Apart from MM1, the only point source that showed water maser activity during both VLA epochs is MM5. The ALMA SiO emission associated with MM5 shows a NE-SW elongation, and we infer this to be the axis of the bipolar outflow driven by the source. While the water maser detected during epoch I (component I-4) is faint and spatially scattered (though it is clearly elongated to the south), the second epoch maser (component II-3-4) has an arc-shaped morphology and, similarly to component I-2, may trace bow-shaped shocks from MM5. The post-flare water masers are probably tracing a bow shock along the jet, directed perpendicular to the pre-flare elongation of the water masers, which therefore could arise close to the disk surface.

Water masers are well known to be variable, and, given the separation of MM1 from the three water maser components associated with MM2, MM4, and MM5, it is quite possible that their behaviour is unrelated to the burst event in MM1. Unfortunately, because of the low flux density and spectral features blending, monitoring of the water maser emission in the source is challenging. No long-term monitoring information on the H_2O maser emission variability is available for the source, which limits our analysis of this option.

On the other hand, the propagation speed of a heatwave of an accretion burst is different in different directions: in the plane of an accretion disk, the wave is slowed by dense structures (as shown in Burns et al. 2020; Bayandina et al. 2022), but in directions where the density of matter is very low, the heatwave speed is supposed to be close to the speed of light in a vacuum. The size of the accretion disk around G358.93−0.03-MM1 is much smaller than the distance to the water masers in the region (radii of ∼0.1″ vs. ∼2″ or ∼6750 vs. ∼13 500 AU, respectively); however, the thermal wave mainly moves through 'empty' space on its way to the water masers. Of particular interest is the fact that, based on this hypothesis, the H_2O maser flare was predicted to start in April (Fig. 3; A.M. Sobolev, priv. comm.). The onset of the accretion burst was assumed to coincide with the methanol maser flare (mid-January 2019; see e.g.,

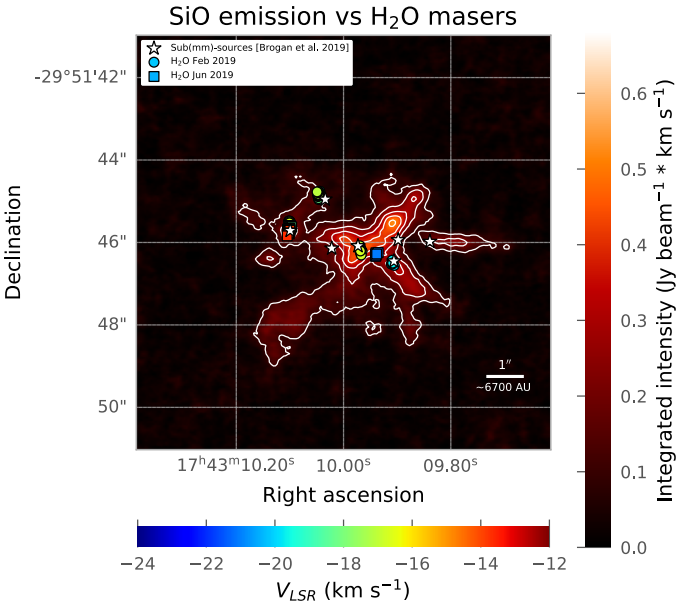

Fig. 10. 22 GHz water maser spot map overplotted on the moment 0 map (integrated over the velocity span of −40 to 3.2 km s^{-1}) of the SiO J = 5–4 emission obtained with ALMA. The contour levels are [1, 2, 3, 4, 5] × 0.1 Jy beam^{-1} km s^{-1}.

Fig. 1 in Bayandina et al. 2022), and, given the H_2O masers' separation from MM1 of ∼2″ (or ∼13 500 AU; see Fig. 4) and the source distance of 6.75 kpc (Reid et al. 2009), the light travel time between MM1 and the water maser positions was supposed to be ∼3 months.

Under such an assumption, the far-infrared emission from MM1 has reached the disk or envelope of other YSOs in the region and has increased the gas temperature and inner turbulence, thus disrupting the velocity coherence for water maser emission (if arising close to the disk surface). Assuming a disk-wind origin for the water masers, a general interpretation might be that the increased temperature and turbulence of the envelope or disk owing to the accretion burst radiation has quenched the (slower) water masers near the YSOs, allowing only for those that could be associated with (faster) shocks at greater distances along the jet or outflow. The detection of several water maser flares (Fig. 3) may be due to the fact that the thermal wave is decelerated in different dense formations, its propagation is not rectilinear (the direction changes), and the heating of the water maser region by the radiation of an accretion burst can occur several times.

We note that the behaviour of the H_2O masers in previously known sources of MYSO accretion bursts was proposed to be explained by the propagation of the burst radiation along the outflow cavities (see Brogan et al. 2018 for NGC6334I-MM1 and Hirota et al. 2021 for S255 NIRS 3). In the case of S255 NIRS 3, even the presence of H_2O masers pumped by radiation (theoretically predicted by Gray et al. 2016) has been suggested (Hirota et al. 2021).

5. Conclusions

Two epochs of VLA imaging of the 22 GHz water maser emission and continuum in the *C*, *Ku*, and *K* bands were performed for the massive star-forming region G358.93−0.03.

1. A drastic change in the distribution of the 22 GHz water masers in the region is found: four spatial maser components are detected during epoch I, and only two during epoch II.
2. The 22 GHz water maser associated with the source of the accretion burst, MM1, traces a jet (outflow) oriented towards the observer with partly overlapping lobes in the plane of the sky.
3. During epoch I, only the blueshifted lobe of the H_2O jet in MM1 is detected.
4. During epoch II, both blueshifted and redshifted lobes of the MM1 jet are detected, indicating the change in the source environment properties to the ones favourable for H_2O maser emission.
5. The extinction of the H_2O masers associated with the MM1 neighbouring continuum sources during epoch II is assumed to indicate a large-scale effect of an accretion event on the host region.
6. Continuum emission associated with the hot core G358.93−0.03-MM3 is detected in all observed frequency bands.

The presented VLA study of the 22 GHz water masers in the accretion burst source G358.93−0.03 illustrated the great importance of observing ejection tracers in the aftermath of an accretion burst, since they not only probe the environment of the central source, but can also reveal possible large-scale burst effects on the entire host region.

Acknowledgements. The Ibaraki 6.7-GHz Methanol Maser Monitor (iMet) program is partially supported by the Inter-university collaborative project "Japanese VLBI Network (JVN)" of NAOJ and JSPS KAKENHI Grant Numbers JP24340034, JP21H01120, and JP21H00032 (YY). The National Radio Astronomy Observatory is a facility of the National Science Foundation operated under cooperative agreement by Associated Universities, Inc. This paper makes use of the following ALMA data: ADS/JAO.ALMA#2019.1.00768.S. ALMA is a partnership of ESO (representing its member states), NSF (USA) and NINS (Japan), together with NRC (Canada), MOST and ASIAA (Taiwan), and KASI (Republic of Korea), in cooperation with the Republic of Chile. The Joint ALMA Observatory is operated by ESO, AUI/NRAO and NAOJ. In addition, publications from NA authors must include the standard NRAO acknowledgement: The National Radio Astronomy Observatory is a facility of the National Science Foundation operated under cooperative agreement by Associated Universities, Inc. A.M.S. acknowledges support by the Ministry of Science and Higher Education of the Russian Federation under the grant 075-15-2020-780. A.C.G. acknowledges support by PRIN-INAF-MAIN-STREAM 2017 "Protoplanetary disks seen through the eyes of new-generation instruments" and by PRIN-INAF 2019 "Spectroscopically tracing the disk dispersal evolution (STRADE)".

References

Bayandina, O. S., Brogan, C. L., Burns, R. A., et al. 2022, AJ, 163, 83
Breen, S. L., Sobolev, A. M., Kaczmarek, J. F., et al. 2019, ApJ, 876, L25
Brogan, C. L., Hunter, T. R., Cyganowski, C. J., et al. 2018, ApJ, 866, 87
Brogan, C. L., Hunter, T. R., Towner, A. P. M., et al. 2019, ApJ, 881, L39
Burns, R. A., Handa, T., Imai, H., et al. 2017, MNRAS, 467, 2367
Burns, R. A., Sugiyama, K., Hirota, T., et al. 2020, Nat. Astron., 4, 506
Burns, R. A., Kobak, A., Garatti, A. C. O., et al. 2022, in European VLBI Network Mini-Symposium and Users' Meeting 2021, 19
Caratti o Garatti, A., Stecklum, B., Garcia Lopez, R., et al. 2017, Nat. Phys., 13, 276
Cesaroni, R., Moscadelli, L., Neri, R., et al. 2018, A&A, 612, A103
Chen, X., Sobolev, A. M., Ren, Z.-Y., et al. 2020, Nat. Astron., 4, 1170
Chibueze, J. O., MacLeod, G. C., Vorster, J. M., et al. 2021, ApJ, 908, 175
Crimier, N., Ceccarelli, C., Alonso-Albi, T., et al. 2010, A&A, 516, A102
Gray, M. D., Baudry, A., Richards, A. M. S., et al. 2016, MNRAS, 456, 374
Hirota, T., Cesaroni, R., Moscadelli, L., et al. 2021, A&A, 647, A23
Hunter, T. R., Brogan, C. L., MacLeod, G., et al. 2017, ApJ, 837, L29
MacLeod, G. C., Smits, D. P., Goedhart, S., et al. 2018, MNRAS, 478, 1077
MacLeod, G. C., Sugiyama, K., Hunter, T. R., et al. 2019, MNRAS, 489, 3981
MacLeod, G. C., Smits, D. P., Green, J. A., & van den Heever, S. P. 2021, MNRAS, 502, 5658
Meyer, D. M. A., Vorobyov, E. I., Elbakyan, V. G., et al. 2019, MNRAS, 482, 5459
Ott, M., Witzel, A., Quirrenbach, A., et al. 1994, A&A, 284, 331
Proven-Adzri, E., MacLeod, G. C., Heever, S. P. v. d., et al. 2019, MNRAS, 487, 2407
Reid, M. J., Menten, K. M., Zheng, X. W., et al. 2009, ApJ, 700, 137
Reid, M. J., Menten, K. M., Brunthaler, A., et al. 2014, ApJ, 783, 130
Sobolev, A. M., Bisyarina, A. P., Gorda, S. Y., & Tatarnikov, A. M. 2019, Res. Astron. Astrophys., 19, 038
Stecklum, B., Wolf, V., Linz, H., et al. 2021, A&A, 646, A161
Sugiyama, K., Saito, Y., Yonekura, Y., & Momose, M. 2019, ATel, 12446, 1
Szymczak, M., Olech, M., Wolak, P., Gérard, E., & Bartkiewicz, A. 2018, A&A, 617, A80